Evidence for crustal seismic anisotropy at the InSight lander site

Jiaqi Li [a,*], Caroline Beghein [a], James Wookey [b], Paul Davis [a], Philippe Lognonné [c], Martin Schimmel [d], Eleonore Stutzmann [c], Matthew Golombek [e], Jean-Paul Montagner [c], William Bruce Banerdt [e]

[a] Department of Earth, Planetary, and Space Sciences, University of California, Los Angeles, CA 90095, USA
[b] School of Earth Sciences, University of Bristol, Bristol, UK
[c] Université de Paris, Institut de physique du globe de Paris, CNRS, Paris, F-75005, France
[d] Geosciences Barcelona - CSIC, Barcelona, Spain
[e] Jet Propulsion Laboratory, California Institute of Technology, Pasadena, CA 91109, USA

ARTICLE INFO

ABSTRACT

We analyzed broadband and low-frequency events recorded on Mars and made the first detection of horizontally polarized shear wave reflections, which help constrain the crustal structure at NASA's InSight lander site. Coherent signals from five well-recorded marsquakes appear to be independent of the focal depth and are consistent with SH-wave reflections off the topmost crustal interface (8 ± 2 km). This phase confirms the existence of the $\sim$8 km interface in the crust and the large wave speed (or impedance) contrast across it. The range of acceptable parameters determined from the detected SH-wave reflections differs from the majority of the vertically polarized shear wave models resulting from a previous receiver function study, indicating that the velocity of the vertically polarized waves is larger than that of horizontally polarized waves. We propose that this inconsistency results from the presence of seismic anisotropy within the top crustal layer at the lander site. Modeling results show that dry- or liquid-filled cracks/fractures and igneous intrusions can reproduce the observed radial anisotropy.

© 2022 Elsevier B.V. All rights reserved.

1. Introduction

Martian crustal structure can reveal how the planet differentiated and evolved over geological times (Hauck and Phillips, 2002; Plesa et al., 2018). After the landing of NASA's InSight mission (Fig. 1a) in November 2018 (Banerdt et al., 2020), data from the Seismic Experiment for Interior Structure (SEIS, Lognonné et al., 2019) were collected and hundreds of events have been recorded. Recent receiver function (hereafter, RF) studies (Lognonné et al., 2020; Knapmeyer-Endrun et al., 2021) and autocorrelation analyses (Compaire et al., 2021; Schimmel et al., 2021; Knapmeyer-Endrun et al., 2021) provide constraints on the crustal thickness and structure beneath the InSight landing site. It was shown that the crust is characterized by interfaces at 8 ± 2 km and 20 ± 5 km depth. A third interface may also be present at 39 ± 8 km depth, implying two possible crustal thicknesses. Although the methods employed were effective at providing the first seismic model of the Martian crust, finding additional seismic phases would help reduce the size of the model space, further constrain the crustal thickness, and possibly reveal new features.

Following the direct S-wave generated by teleseismic events, observable phases include reflected waves bouncing between the free surface and crustal discontinuities on both the source- and the receiver-side. For horizontally polarized incoming S-waves (SH) (Fig. 1c), there are no P-wave transmissions on horizontal discontinuities and SH-wave reflections are the dominant phases on the tangential component of the seismogram. On Earth, these topside SH-reverberations were utilized to image discontinuities in the upper mantle (Shearer and Buehler, 2019; Liu et al., in preparation) and the lithosphere (Liu and Shearer, 2021). The differential travel-time between the direct SH phase (Ss) and the SH-wave reflection (SsSs) can be used to constrain the S-wave speed and thickness of the layer based on ray theory:

$$T_{SsSs-Ss} = 2H\left(\frac{1}{V_{SH}^2} - p_{SH}^2\right)^{1/2} \qquad (1)$$

where p_{SH} is the horizontal slowness (ray parameter) of the incident SH-wave, V_{SH} is the average SH-wave speed in the layer, and H is the overall thickness of that layer.
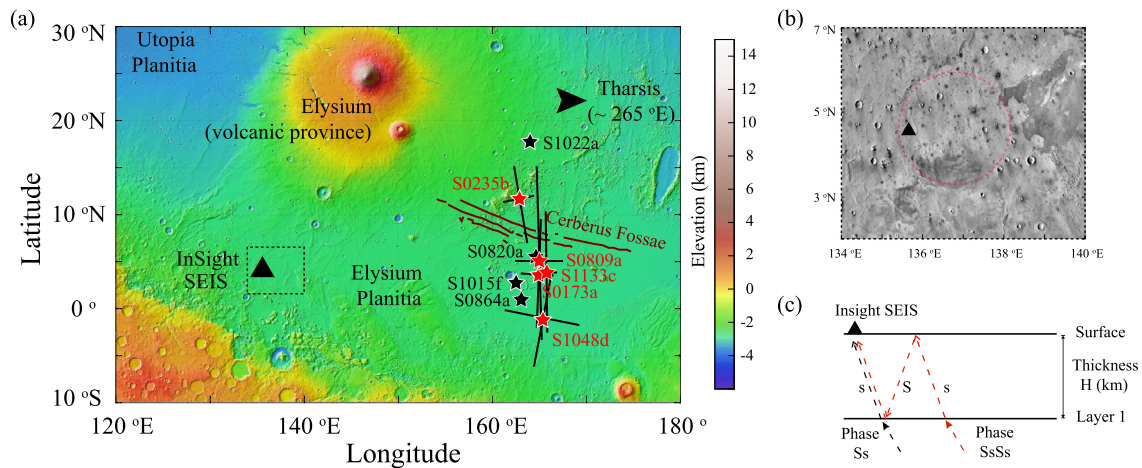
Fig. 1. (a) Topographic map from Mars Orbiter Laser Altimeter (MOLA, Smith et al., 2001) near the InSight lander (black triangle). The red and black stars mark the nine quality-A events selected for this study. The red stars denote the five marsquakes used in the inversion and the black error-bars indicate the uncertainties in both their epicentral distance and back azimuth. The black stars show the other four quality-A events. (b) The infrared daytime image from the Thermal Emission Imaging System (THEMIS-IR, Edwards et al., 2011) of the region (marked by dashed box) in (a). The quasi-circular depression, interpreted to be a buried, degraded impact crater (∼175 km diameter) is indicated by the dotted red circle, with the InSight lander (black triangle) near the western edge of the crater (Golombek et al., 2018). (c) Ray paths of the SH-wave reflection from a planar, incident teleseismic SH-wave near the InSight SEIS instrument. The direct phase Ss is in black and the reflected phase is in red. (For interpretation of the colors in the figure(s), the reader is referred to the web version of this article.)

Compared with the more widely used RF methods (e.g., Langston, 1979), SH-wave reflections can better constrain the depth of the reflector due to the relatively larger travel time differences (Liu and Shearer, 2021). In addition, unlike the RF technique, which is sensitive to the wave speed ratio between P- and SV-waves (vertically polarized shear waves), SH-wave reflections can directly constrain absolute SH-wave speeds.

In this paper, we focus on the shallow layer, at 8 ± 2 km (Lognonné et al., 2020; Knapmeyer-Endrun et al., 2021) of the Martian crust at the lander site, hereafter referred to as Layer 1. Not only is this layer the least contaminated by interferences from source-side scattering and other reflections from deeper layers (see section 4.1), but the previously observed large wave speed jump at the interface (up to +40%, Knapmeyer-Endrun et al. (2021)) can generate strong reflected phases that are observable with a single event without the need for stacking. In addition, any constraints on Layer 1 would provide useful information for future studies on the deeper layers.

2. Data and methods

From Sol 105, when the first low-frequency marsquake was recorded by SEIS, to Sol 1133, a total of 86 broadband and low-frequency events were detected (Clinton et al., 2021; InSight Marsquake Service, 2020, 2021a, 2021b, 2022a, 2022b). Eleven of them are rated as quality-A, as defined by Clinton et al. (2021), with constraints on both their epicentral distance and back azimuth. We analyzed the waveforms (InSight Mars SEIS Data Service, 2019) from all the quality-A marsquakes with epicentral distances smaller than 60 degrees (9 out of 11, see Table S1) to avoid interferences with mantle triplications generated by the olivine-to-wadsleyite phase transition that occurs at around 1000 km depth on Mars (Stähler et al., 2021).

We note that since the SEIS instrument operates in an extremely harsh environment (both wind and temperature, e.g., Lognonné et al., 2020, Ceylan et al., 2021), internal thermal stresses from diurnal temperature variations can generate transient one-sided pulses, hereafter referred to as glitches (Scholz et al., 2020). To minimize their effect, we hierarchically detected the glitches in the continuous waveform and removed them on the U, V, W components using a synthetic glitch template (Scholz et al., 2020).

For the deglitched dataset (provided as supplementary data), which had a sampling rate of 20 samples per second, we removed the instrument response, with a pre-filtering from 0.01 to 8 Hz, to get the ground motion records. Then, we rotated the coordinates from the original UVW to NEZ using ObsPy (Beyreuther et al., 2010). To analyze SH-wave reflections, we need to use data on the tangential (T) component, which required back azimuth information since the back azimuth is also defined as the angle to rotate the N and E components into R and T components. We estimated the back azimuth based on the analysis of P-wave polarization with data filtered from 2 s to 5 s (Fig. 2 and Fig. 3). For these nine quality-A events, our derived back azimuths are all within the estimated ranges from the InSight Marsquake Service (MQS) (2020, 2021a, 2021b, 2022a, 2022b). We further tested that uncertainties in the back azimuth do not influence our SH-wave arrivals (see section 4.2 and Fig. S1).

2.1. Data analysis

In the present study, we calculated synthetic SH waveforms (on the tangential component) for all 40,000 most likely P-wave RF crustal models obtained by Knapmeyer-Endrun et al. (2021). The synthetics were calculated with the propagator matrix method (Kennett, 2009) using ray parameters estimated from the Mars mantle model of Stähler et al. (2021). Synthetic waveforms indicate that the predicted SH-wave reflection off Layer 1 has a negative polarity compared to the direct SH phase, and arrives at around 9.5 ± 1.5 seconds for events with epicentral distances of about 30 degrees (e.g., see Fig. 4a2). Thus, for the data, we aligned and normalized the T-component seismogram according to the direct SH phase (multiplied by -1 to make the polarity of the direct SH phase positive, if needed) for each event, and searched for a negative phase (Shearer, 2019) in a wider time-window of 9.5 ± 3.0 seconds. We note that we chose a relatively broad filtering band to maintain the original appearance of the data as much as possible.

Out of the nine selected events, five (S0235b, S1133c, S0173a, S1048d, and S0809a) display clear negative phases indicative of SH reflections off Layer 1. For instance, broadband event S0235b (Fig. 2a1) shows a clear negative signal at around 10.2 s after the direct SH phase. It also displays complexity in the source time
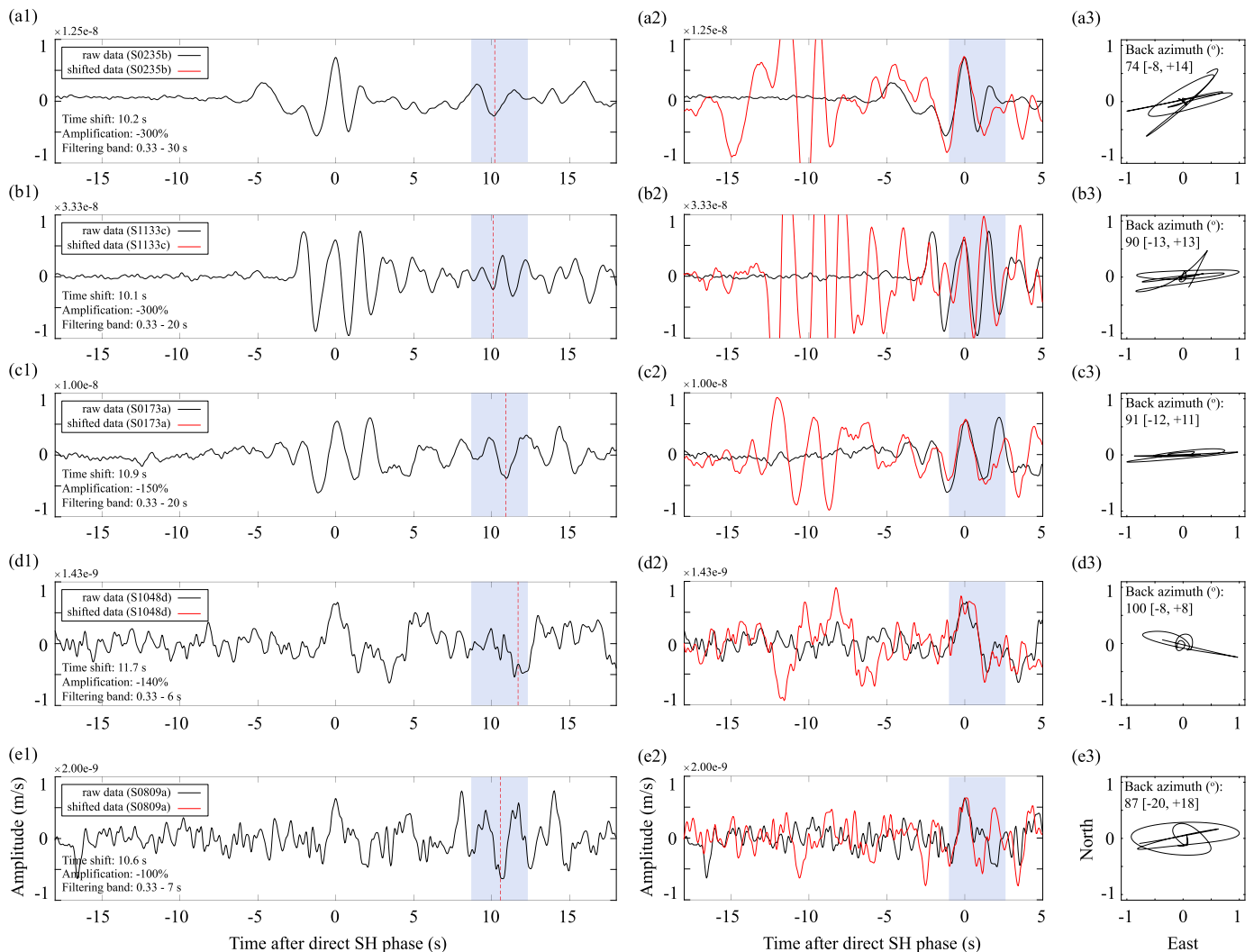
Fig. 2. Waveforms for events S0235b, S1133c, S0173a, S1048d, and S0809a. (a1) The black waveform is the velocity data for event S0235b on the tangential (T) component. The shaded purple region and the dashed red line mark the arrival of the negative signal at 10.2 s. The filtering band is denoted in the lower left corner. (a2) Comparison between the original waveform (in black), and the shifted trace (by −10.2 s) with its amplitude amplified by −300% (in red). With a time shift and amplitude amplification, the negative phase (originally at 10.2 s) overlaps with the source wavelet. (a3) P-wave particle motion (black curves) for event S0235b (in a 6-s time window around the direct P-wave arrival). The back azimuth and its uncertainties from MQS (Clinton et al., 2021; InSight Marsquake Service, 2021a, 2021b, 2022a, 2022b) are denoted in the upper left corner. Same analysis for event (b1-b3) S1133c, (c1-c3) S0173a, (d1-d3) S1048d, and (e1-e3) S0809a.

function over a broad frequency range (from 30 s to 3 Hz) with two separate positive phases of different amplitudes at −5 s and 0 s. If we shift the original trace (the black waveform in Fig. 2a1 and Fig. 2a2) by 10.2 s and amplify its amplitude by −300% (the red waveform in Fig. 2a2), the phase originally at 10.2 s fits the source wavelet (from −1 to 1 s) very well (with a cross-correlation coefficient of 0.92). We note that a negative amplification factor (i.e., −300%) accounts for the polarity change for the topside SH-reflection off Layer 1 (Shearer, 2019). More surprisingly, the entire complex source wavelet (from −5 to 2 s) is well-matched (with a cross-correlation coefficient of 0.75). This similarity with the source wavelet indicates that this negative signal at around 10 s, on the tangential component, is likely a reflected phase, generated either at the receiver side or the source side.

For broadband event S1133c (from 20 s to 3 Hz), there is also a clear signal at around 10 s. When a similar time shift of 10.1 s and an amplification factor of −300% is applied to the original trace (Fig. 2b), the direct SH-phase (although with multiple peaks) can be matched with a cross-correlation coefficient of 0.71. Low-frequency event S1048d (from 6 s to 3 Hz, see Fig. 2d) also exhibits

a negative phase at around 11.7 s, although there is another positive signal at around 5 s which might be the depth phase from the source side (see Discussion). Nevertheless, this positive signal at around 5 s does not interfere with the negative phase at around 11.7 s, and the similarity between the negative phase (at around 11.7 s) and the source wavelet (from −1 to 3 s) is high (with cross-correlation coefficient of 0.89). Low-frequency events S0173a (from 30 s to 3 Hz, see Fig. 2c) and S0809a (from 7 s to 3 Hz, see Fig. 2e) coherently show negative phases at 10.9 s and 10.6 s, respectively. However, besides a positive phase at around 5 s (like S1048d), there are other pulses between 10 s and 15 s which will probably be overlapped with the negative phase at around 11 s.

The other four quality-A events (S1015f, S1022a, S0864a, and S0820a) exhibit hints of negative phases at similar arrival times as the events discussed above and do not violate the observations. However, they generally behave less well. For broadband event S1015f (Fig. 3a), the possible source wavelet is too complex (including four phases at −3 s, 0 s, 2 s, and 4 s): although the last three source wavelets can be matched by the negative wave trains beginning at around 10.7 s, the corresponding reflected phase for
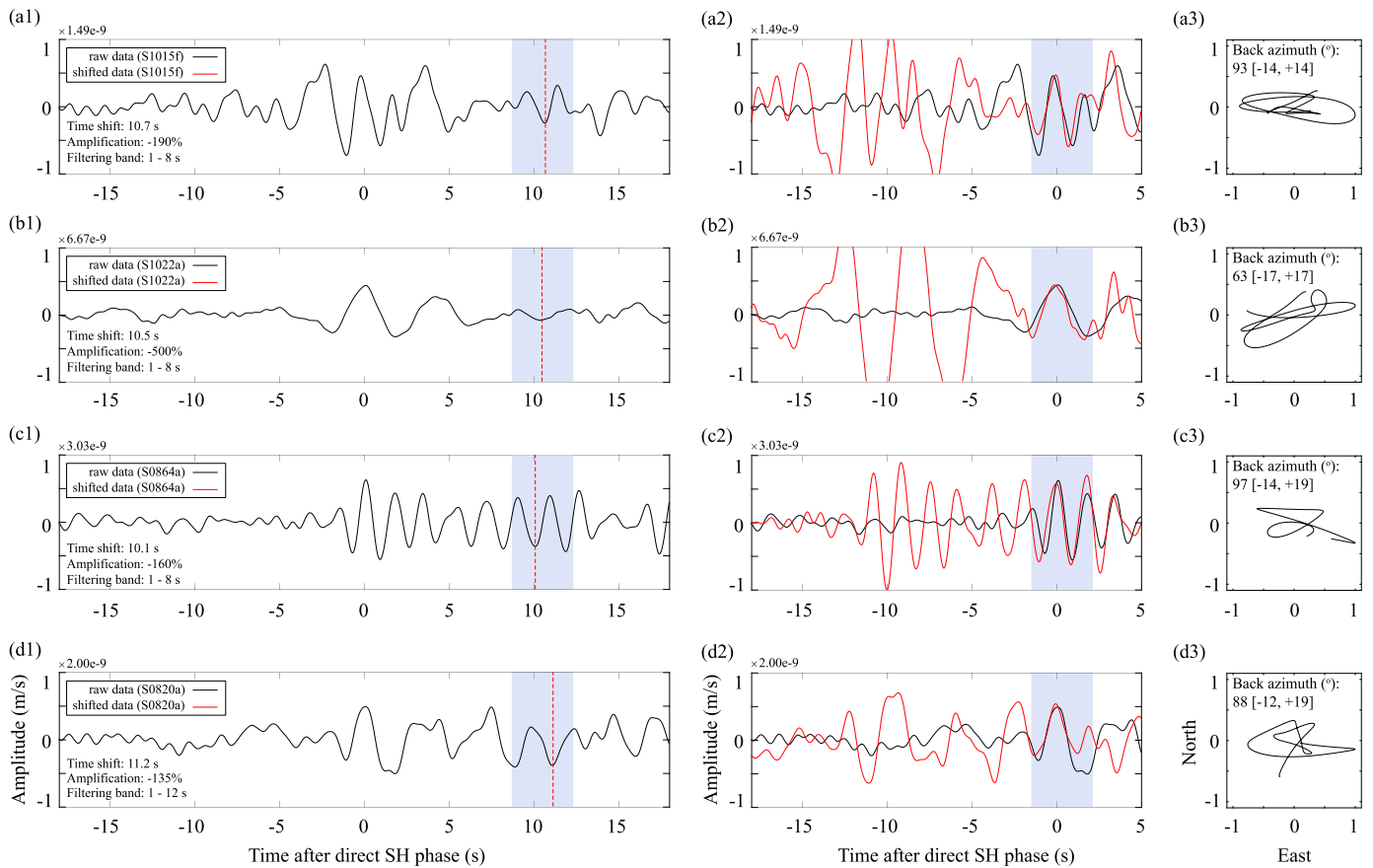
Fig. 3. Waveforms for events (a1-a3) S1015f, (b1-b3) S1022a, (c1-c3) S0864a, and (d1-d3) S0820a. The layout is the same as Fig. 2.

the first source wavelet (−3 s) cannot be found and is probably buried in the long source time function (duration of about 10 s). Low-frequency event S1022a (Fig. 3b) displays a lack of high-frequency energy, and broadband event S0864a (Fig. 3c) as well as low-frequency event S0820a (Fig. 3d) present strong oscillations after the direct SH waves.

To summarize, S0235b is the best event among all nine quality-A events, with a clear negative phase at 10.2 s, and there are no other phases in between. Events S1133c, S0173a, S1048d, and S0809a also show a consistent negative phase at 10 s to 12 s, although the source wavelets for S1133c and S0173a display multiple peaks that hinder the waveform matching. There is also contamination from noise or other unknown phases which might affect the amplitude and arrival time. Events S1015f, S1022a, S0864a, and S0820a display similar negative phases, but they were discarded due to their lower quality regarding the detection of the SH reflected waves. Because the negative phase observation at around 10 s to 12 s is consistent for all nine quality-A events, it is more likely to come from a common crustal structure (Layer 1) at the receiver side than to reflect a common focal depth for all these events (see section 4.1).

We note that the different behaviors of the quality-A events are understandable because event quality was defined in terms of the performance regarding event location (Clinton et al., 2021). Specifically, achieving quality-A requires both clear P and S phases and polarization, yielding clear epicentral distance and back azimuth, respectively. Therefore, the definition of a quality-A event takes only the direct S phase into account, and does not consider the source time function (e.g., S1015f and S1022a), possible depth phases (e.g., S0173a, S0809a, and S1048d), or oscillations after the direct phase (e.g., S0820a and S0864a).

2.2. Constraints from SH-wave reflections

We focus on waveforms from events S0235b, S1133c, S0173a, S1048d, and S0809a to constrain the SH-wave speed and thickness of Layer 1. For the synthetic seismogram, since each event has a distinct source time function, we convolved the original synthetic output (delta function as the source wavelet) with the assumed source wavelet (from −7 to 3 s of the data).

Equation (1) shows that trade-offs exist between model parameters (SH-wave speed and thickness of Layer 1) and therefore the solution is non-unique. To find all acceptable models, we sampled the SH-wave speed (from 0.8 km/s to 2.4 km/s with an interval of 0.01 km/s) and thickness (from 4 km to 14 km with an interval of 0.05 km) of Layer 1. At each grid cell, we calculated synthetic waveforms, convolved the synthetics with their source wavelet, and finally derived the cross-correlation coefficient between the data and the synthetics. The cross-correlation maps are shown in the top panels of Fig. 4. Models in the red regions have higher cross-correlation coefficients and are thus more acceptable than models in the blue regions. One of those models was selected (represented by the black star) and the corresponding waveform is shown in the bottom panels of Fig. 4 to illustrate that they predict waveforms that are similar to the data. The cross-correlation maps for these five events are similar, especially the first-order pattern. They all show a sub-linear region on the diagonal, consistent with the ray-theory-based equation (1). We note that there are multiple red regions in the cross-correlation maps for S1133c (Fig. 4b1) and S0173a (Fig. 4c1). Those features are due to the multiple peaks in the source time functions of those two events, which are not observed in other events with relatively simple source time functions. Other differences between the cross-correlation maps might
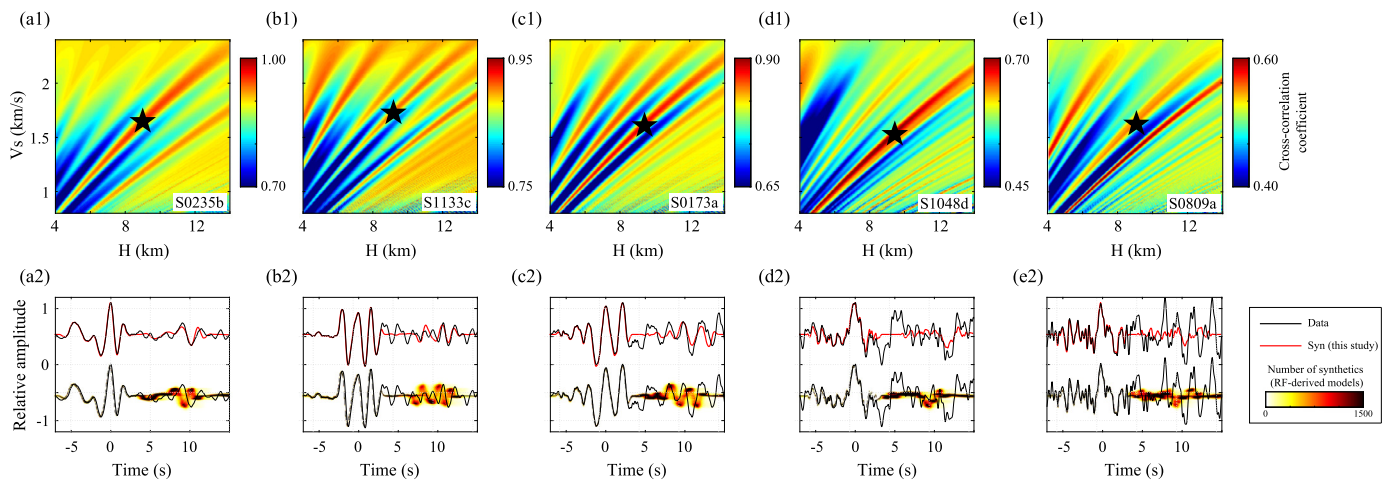
Fig. 4. Cross-correlation coefficients for combinations of SH-wave velocity and layer thickness and comparison between observations and synthetic waveforms. (a1) Cross-correlation map for event S0235b. The black star marks the model used to calculate the synthetics in (a2). (a2) The two traces at the top are the data (in black) and the synthetics (in red, the corresponding model is indicated by the black star in a1) for event S0235b on the tangential (T) component. The two traces at the bottom are the data (in black) and the synthetics (colorscales denote the number of models) calculated using 40,000 models from the RF study (Knapmeyer-Endrun et al., 2021). Same analysis for event (b1-b2) S1133c, (c1-c2) S0173a, (d1-d2) S1048d, and (e1-e2) S0809a.
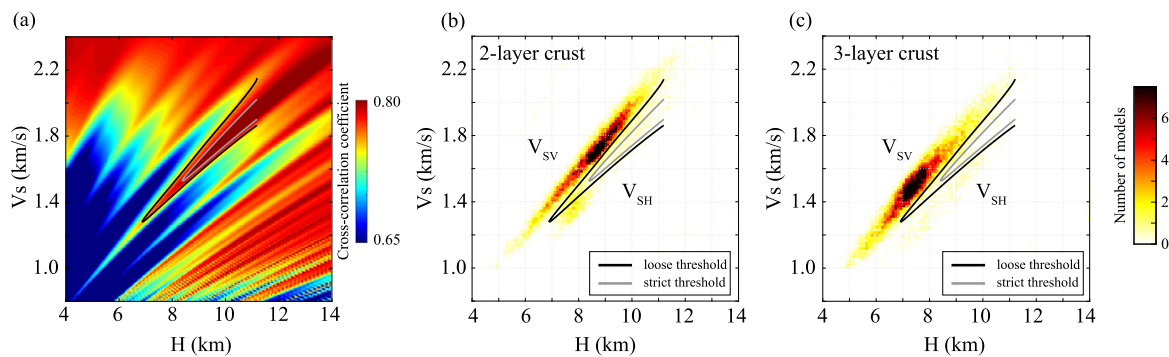
Fig. 5. S-wave speed models for Layer 1. (a) The average cross-correlation map for the SH-wave reflections. The black and grey curves mark the acceptable model regions with loose and strict thresholds, respectively. (b) Colored dots represent the 20,000 models from the receiver functions study (Knapmeyer-Endrun et al., 2021) for the 2-layer crustal case. Color indicates the number of models at each grid point. (c) Same as (b) for the 3-layer crustal case.

be partly due to different noise levels, frequency bands, source-side scattering, epicentral distances, and possible interference from other phases.

To enhance the coherent features, we averaged these cross-correlation maps with different weights (see Discussion). The weights for S0235b, S1133c, S0173a, S1048d, and S0809a are 1.0, 0.2, 0.2, 0.5, and 0.2, respectively. We note that events S1133c, S0173a, S1048d, and S0809a are down-weighted because of multiple peaks in the source wavelet or interferences from other phases, and events S1133c, S0173a, and S0809a are further down-weighted due to their similar back azimuths. The average cross-correlation map is shown in Fig. 5a. To extract the acceptable region of the model space (the red region on the diagonal), we set both a strict cross-correlation coefficient threshold of 0.785 (the grey curve in Fig. 5a) and a slightly looser threshold of 0.765 (the black curve in Fig. 5a). We note that we did not pick the arrival time of the phases nor did we use equation (1) to calculate the corresponding wave speed and the layer thickness. Instead, we chose the threshold of the cross-correlation map to extract acceptable model regions. Cross-correlation maps are more reliable to measure travel time differences since multiple sources of uncertainties, such as the noise in the data, the duration of the pulse, and even finite-frequency effects, are automatically included.

We tested several thresholds and compared them with predictions from ray theory to ensure our analyses are reliable. We found that if we consider a value smaller than 0.765, the contour (Fig.

S2c) begins to significantly deviate from the trend along the diagonal and is inconsistent with the prediction from equation (1).

3. Results

3.1. S-wave speed

Our study provides constraints on SH-wave velocity using SH-wave reflections, which can be compared to the 20,000 acceptable 2-layer and 3-layer crustal models of the Knapmeyer-Endrun et al. (2021) RF study. Here, we plotted the distribution of S-wave speed and thickness for the top layer using those 20,000 models in the 2-layer and 3-layer models obtained with RF (Fig. 5b and 5c, respectively). In both cases, the models are roughly located along a sub-linear trend reflecting the trade-offs between the wave speed and layer thickness.

Assuming the P-to-s converted phases (from the RF study) and the SH-wave reflections are generated from the same interface (discussion of this assumption can be found in section 4.3), we superimposed the acceptable model space regions determined from our SH-wave reflections analysis for the strict and loose thresholds (e.g., grey and black lines in Fig. 5b, respectively). Results show that the range of acceptable parameters determined from our SH-wave analysis does not intersect with the majority of the 20,000 models from Knapmeyer-Endrun et al. (2021), for both the strict and loose thresholds. More specifically, for each layer thickness,
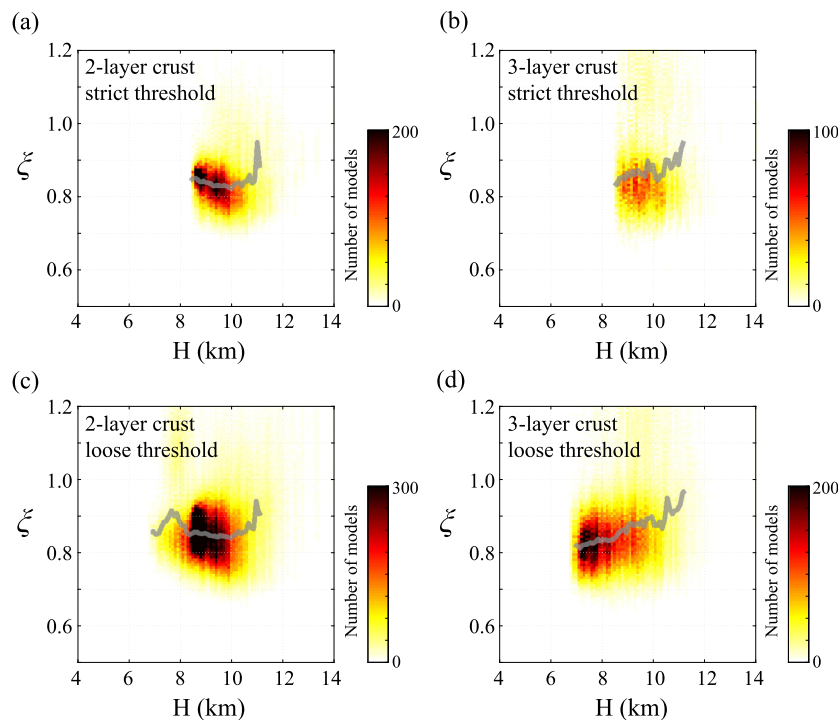
Fig. 6. Distribution of the radial anisotropy coefficient $\xi = (V_{SH}/V_{SV})^2$ in Layer 1. (a) This is for the 2-layer crustal case in the receiver function study (Knapmeyer-Endrun et al., 2021) using the strict SH-wave threshold. The color scale indicates the number of models at each grid point. The solid grey line mark the average value of the anisotropy coefficient. (b) The 3-layer crustal case with the strict SH-wave threshold. (c) The 2-layer crustal case with the loose SH-wave threshold. (d) The 3-layer crustal case with the loose SH-wave threshold.

the acceptable S-wave speeds from the SH-wave reflections are systematically lower than those from the RF study. Consistently, the predicted arrival times (at around 9 seconds) with the RF-derived models (the bottom panels of Fig. 4) are also earlier than the signals we observed at around 11 seconds.

We propose that this inconsistency results from the presence of seismic anisotropy within crustal Layer 1 at the lander site since our SH-wave reflections study constrains horizontally polarized shear-wave velocity (V_{SH}) whereas the RFs analysis constrains vertically polarized shear-wave speed (V_{SV}).

For the best event, S0235b, a delay time of 10.2 s, and amplification of -300% are required to match the reflected phase and the direct SH-wave. For the other four events, either complex source wavelets are observed (i.e., S1133c, and S0173a) or very different and suspiciously low amplifications are required (i.e., S0173a, S1048d, and S0809a). Although low weights for the other four events were set during the inversion (Fig. 5a), we performed an additional inversion using only the single event S0235b. Despite the differences in the absolute values of the cross-correlation coefficients, both inversions yield very similar results of $V_{SH} < V_{SV}$ (Fig. 5 and Fig. S3). We also note that most of the other events show larger travel time differences (i.e., 10.1, 10.6, 10.9, and 11.7 s) compared with S0235b (i.e., 10.2 s). Consequently, the currently derived value of V_{SH} (where other events have low weights) can be viewed as a maximum estimation. Therefore, applying different weights (e.g., enlarging the weights for other events) will even lower the value of V_{SH} without changing the conclusion of $V_{SH} < V_{SV}$ (Fig. S4).

3.2. Crustal anisotropy

To quantify the radial anisotropy amplitude, we sampled the V_{SV} and V_{SH} models to calculate the anisotropy coefficient $\xi = (V_{SH}/V_{SV})^2$. In practice, we first extracted V_{SV} and layer thickness of the model at each grid point. Then, for this specific layer

thickness, we sampled V_{SH} between its upper and lower limits (i.e., grey and black lines for the strict and loose thresholds in Fig. 5a, respectively) with an interval of 0.01 km/s and calculated the corresponding ξ values. We did this for all the model grids and derived ξ distribution maps. Fig. 6a and 6b show the ξ distributions with the strict V_{SH} threshold for the 2-layer and 3-layer crust cases, respectively. Similar maps for the loose V_{SH} threshold are shown in Fig. 6c and 6d. For all cases, the ξ values are concentrated between 0.7 and 0.9, corresponding to $V_{SH} < V_{SV}$ with 10% to 30% anisotropy. The mean value and standard deviation of ξ are 0.88 and 0.10, respectively.

In addition to choosing the thickness from the RF models, we performed an additional calculation in which we performed a grid search for all the possible thickness values (with an interval of 0.1 km) and then calculated the anisotropy coefficient for each thickness using the averaged V_{SV} and V_{SH} values from the RF and SH-wave reflection studies, respectively. The average coefficient value (the solid grey curves in Fig. 6) is around 0.85, which falls into the previous range between 0.7 and 0.9.

To determine the reliability of our threshold choices, we tried to find a threshold value in the SH-wave reflection cross-correlation map (Fig. 5a) that would force V_{SH} to be equal to V_{SV}. We found that we would need a threshold lower than 0.65, which deviates significantly from the predictions of ray theory (Eq. (1)). We, therefore, conclude that an isotropic layer is less likely than our solution with $V_{SH} < V_{SV}$.

4. Discussion

4.1. Source-side scattering

Our target structure is the top crustal layer (at 8 ± 2 km depth) beneath the InSight lander. At the receiver side, any free-surface reflections from deeper layers will arrive later and thus fall outside of the window of interest. The only phases that may arrive

earlier are the waves reflected between Layer 1 and the deeper layer (at 20 ± 5 km depth), but the amplitudes of such inter-layer reflections are much smaller than reflections at the free surface (Fig. S5). Therefore receiver-side reflections from deeper layers do not influence our phase identification or the results presented in this study.

Interference, if present, would come from the source side. When the focal depth is shallower or closer to the discontinuity, free-surface reflection at the source side yields similar arrival times as receiver-side reflections (e.g., the SH-wave reflections we studied in this paper). Therefore, deep events are usually preferred for SH-wave reflection studies (Liu and Shearer, 2021). Although there have not yet been conclusive focal depth reports for marsquakes due to the unclear identification of depth phases, most of the detected low-frequency and broadband events are likely deeper than Layer 1 since they do not excite trapped waves (Giardini et al., 2020). Therefore, the possible source-side scattering will not likely arrive at similar times as the receiver-side SH-wave reflections for Layer 1, but the depth of Layer 1 at the source side may differ from the one beneath the SEIS station.

Nevertheless, all events with clear negative signals show coherent arrivals at around 10-11 s (Figs. 2 and 3). This consistency implies that the phases we interpreted to be the SH-wave reflections are not strongly dependent on the focal depths. If the negative phase was a depth phase, all events with different locations (Fig. 1a) would have to have similar focal depths and focal mechanisms to ensure coherent arrival times and polarity. Although we cannot completely rule out this possibility, we think this is less likely since, for example, Brinkman et al. (2021) showed that focal mechanisms and depths differ between S0173a and S0235b.

Besides free-surface reflections, source-side scattering also includes another depth phase that reflects from Layer 1 (underside reflection) at the source side. The arrival and polarity of this underside reflection depend on the focal depth and focal mechanism. This phase may be present between the direct SH wave and the SH-wave reflection. For example, we find a signal at about 5 seconds after the direct SH arrival for events S1048d, S0173a, and S0809a (Fig. 2). We think it is likely to be the underside reflection at the source side for two reasons. First, the amplitudes of inter-layer reflections at the receiver side are much smaller (Fig. S5). Second, the polarity of this phase varies among different events (Fig. b1-e1), probably indicating its dependence on different focal mechanisms. Nevertheless, this positive signal (at about 5 s) does not interfere with the SH-wave reflection at around 10-11 s, and will not significantly influence our analysis. However, when source-side scattering (reflections off the free surface or Layer 1) arrives at a similar time as the SH-wave reflection, it contaminates both the arrival time and the amplitude of the negative phase we are interested in. This might explain the amplitude discrepancies between the data and the synthetic SH-wave reflections for some events (e.g., S0173a, and S0809a in Fig. 4).

We note that, in our forward modeling of the synthetic waveforms with planar SH-wave incidence, only receiver-side scattering (e.g., SH-wave reflections and their multiples) is calculated, and source-side scattering is excluded (e.g., depth phases). We specifically chose this computational method because we have very little information on the focal depths and source-side structure. To benchmark our computations, we also calculated the synthetic waveforms using another orthonormal propagator algorithm, QSEIS (Wang, 1999), for events at various depths (from 15 km to 50 km with an interval of 5 km) and then stacked all the QSEIS-synthetics. We found that the SH-wave reflection in the stacked waveform is very similar to the one calculated with planar wave incidence (Fig. S6a). Therefore, the planar S-wave incidence technique used here is reliable, especially since our analysis is based on the average cross-correlation maps from five different events.

4.2. Uncertainties

Various factors can contribute to model uncertainties. For instance, glitches, if present in the time window of the S-wave reflections, will affect our analysis and results. Thus, to fully understand their possible influence, we analyzed both the raw data and deglitched data (Fig. S7). We found that none of the nine events used show any glitch within the selected time window (from −18 to 18 s). Glitches, therefore, do not affect the results presented here.

Source parameters (e.g., focal depths and focal mechanism) influence the arrival time and amplitude of the entire wave train. However, they likely do not strongly influence our results because they have a similar impact on both the direct phase and the receiver-side reflections due to their almost identical take-off angles and identical ray paths away from the receiver.

For similar reasons, attenuation in the deeper crust and mantle will affect the direct phase and reflections in the same way. Therefore, mantle attenuation only slightly influences our results when we normalize the trace to the direct phase. Only the attenuation in Layer 1 will influence them differently. However, due to the very short propagation distance within Layer 1, even a highly-attenuating model (e.g., with Qs equals 150) does not change the reflected phases significantly (Fig. S6b). The same holds for the influence of possible errors in the mantle model.

There are also uncertainties (less than 5 degrees) in the epicentral distance of the quality-A marsquakes we utilized due to the uncertainties in the P- and S-phase picking (Clinton et al., 2021; InSight Marsquake Service, 2020, 2021a, 2021b, 2022a, 2022b) and in the Mars 1-D model. Inaccurate epicentral distance will result in a deviated ray parameter, and this error will propagate into the cross-correlation map, although the influence is subtle within the uncertainty range (Fig. S8). To take this source of uncertainty into account, we chose the minimum and maximum epicentral distances (Clinton et al., 2021; InSight Marsquake Service, 2020, 2021a, 2021b, 2022a, 2022b) to calculate two synthetic waveforms and then derived two cross-correlation maps for each event. Our final cross-correlation map (Fig. 3a) results from the averaging of the cross-correlation maps of these two end-member epicentral distances (Fig. S8) and therefore includes the propagation of uncertainties in the epicentral distance.

There are also uncertainties in the estimated back azimuth, which will influence the SH waveforms on the tangential component (during the rotation from North-East to Radial-Tangential components). We tested that, given the uncertainties in the back azimuth (Clinton et al., 2021; InSight Marsquake Service, 2020, 2021a, 2021b, 2022a, 2022b), the SH-waveform only slightly changes and the arrival time is almost constant (Fig. S1).

4.3. Interface sharpness

Both our results and those from the RF study assume a sharp interface. If this is the case, since the SH-wave reflection and the RF are sampling the same discontinuity at the same depth, the observed $V_{SH} < V_{SV}$ implies anisotropy within Layer 1. If the interface of Layer 1 is gradual (e.g., with a thickness of 2 km), synthetic inversion tests in which we assumed a sharp interface during the inversion show that the RF still samples the mid-point of this gradual interface (Fig. S9a). However, in this case, the inverted depth from the SH-wave reflection is shallower than the mid-point of the gradual interface. This result is consistent with the larger time shift of the SH-wave reflection (Fig. S9b) compared with the almost invisible change of the arrival for the P- to s-wave RF (Fig. S9c). This means that, if the interface is gradual, SH-wave reflection underestimates the depth of Layer 1 compared with RFs. Therefore, the reflection-derived region (V_{SH}) would shift to larger depths

(Fig. 5b, c), which implies an even greater difference between V_{SH} and V_{SV}. Thus, whether the interface of Layer 1 is sharp or gradual, the evidence of $V_{SH} < V_{SV}$ is robust.

4.4. Dipping and curved interface

An alternative to the proposed radial anisotropy to explain the discrepancies between the RF- and reflection-derived V_S models is the existence of a dipping and curved interface because the point where the incident wave enters Layer 1 differs between the SH-wave reflections (Fig. S10a) and the P-wave RFs (Fig. S10b).

Based on ray theory, the horizontal distance between the InSight lander and the point where SH-waves enter Layer 1 is between 1.9 km and 4.2 km. Additionally, the RF samples a region closer to the lander site (Fig. S10b). If we assume that Layer 1 is shallower beneath the lander site, even if it is isotropic ($V_{SH} = V_{SV}$, see Fig. S10c and S10d), models constrained from SH-wave reflections also yield later arrival times (i.e., 10-11 s, shown in Fig. 2) than the RFs-derived models (i.e., 9 s, Fig. 4) since SH-wave reflections are sampling regions farther away from the receiver.

Nevertheless, given the size of the S-wave Fresnel zone (about 3 – 8 km) and the shorter distance (< 4.2 km) between the lander and the point where S-waves enter Layer 1, dipping layer or small-scale topography (e.g., curved interface) may have limited influence on the results.

4.5. Seismic anisotropy

The average radial anisotropy coefficient, $\xi = (V_{SH}/V_{SV})^2$, in Layer 1 (at 8 ± 2 km depth) of the Martian crust ranges from 0.7 to 0.9. Similar radial anisotropy observations have been reported in various regions on Earth. For example, a ξ value of 0.8 has been found in the upper crust (top 5 km) in Iceland (Volk et al., 2021), and lower SH-wave speeds by at least -12% compared with SV-waves have been observed in the middle crust (5 – 20 km) of southern Madagascar (Dreiling et al., 2018). Another SH-wave speed reduction of -5% has been identified in the top 8 km of the crust in the eastern part of the Variscan orogeny (Acevedo et al., 2022).

The amplitude ($\xi < 1$) of the detected anisotropy may be the seismic signature of vertical dry or gas-filled fractures due to the extension of impact-related stresses, normal faults due to crustal extension, or vertical liquid intrusions such as melt pockets, magmatic dykes, and water-saturated fractures (Bastow et al., 2010; Dreiling et al., 2018; Volk et al., 2021). We prefer to consider water-saturated (rather than ice-filled) fractures because Manga and Wright (2021) found that there is no cryosphere beneath the InSight lander site since the S-wave speed from the RF study (Knapmeyer-Endrun et al., 2021) is too low to be ice-saturated.

On Mars, the study of Knapmeyer-Endrun et al. (2021) suggests an upper crust with very low density for the top 10 km (<2000 kg/m^3, constrained from RF waveforms data), increasing at depths greater than 10 km to values close to those (~2600 kg/m^3) proposed by Goossens et al. (2017) based on orbital gravity data. Such a low density, if confirmed, could indicate the presence of less dense sedimentary rocks (Pan et al., 2020) and/or rocks with porosity in Layer 1 (e.g., Lognonné et al., 2020; Knapmeyer-Endrun et al., 2021). Increased porosity is compatible with large impact (e.g., Johnson et al., 2021) and associated fractures or pore space as possible candidates that could generate the observed radial anisotropy. These effects can furthermore be amplified near the equator and in the vicinity of the InSight landing site, where ground ice is not stable (e.g., Clifford et al., 2010), which will lead ultimately to large, gas-filled cracks and connected porosity.

In addition to radial anisotropy, which quantifies the difference in wave speed between the vertical and horizontal direction, a medium can be azimuthally anisotropic, in which case the wave speed varies with the azimuth of propagation. Constraining both types of anisotropy is essential to obtain a more complete description of the elastic properties of the planet interior. With the current approach, which compares SV- and SH-wave speeds from RF and SH-reflection analysis to infer seismic anisotropy, a range of back azimuths is required to constrain azimuthal anisotropy. However, all the quality-A marsquakes with known back azimuth occurred roughly to the east of the lander, making a robust estimate of azimuthal anisotropy impossible at this point.

Shear-wave splitting with a single measurement could provide insights into azimuthal anisotropy (e.g., Silver and Chan, 1988). However, waveform distortions, probably due to the near- or post-critical reflection at the surface (e.g., Savage, 1999), prevent us from measuring shear-wave splitting with traditional methods (see Fig. S11 and S12, and discussion can be found in the supplementary material).

4.6. Anisotropy modeling

To model the observed radial anisotropy, without loss of generality, we consider a situation of preferred alignment of intrusions, which can represent various situations (e.g., intrusions of gas- or liquid-filled space, or melt pockets with different physical parameters). The model setup is shown in Fig. 7a: an isotropic background matrix ($V_P = 2.8$ km/s, $V_S = 1.4$ km/s) is reinforced with isotropic oblate spheroidal intrusions with a horizontal symmetry axis, resulting in a composite that is (horizontally) transversely isotropic. We used an analytical solution to determine the elasticity matrix of the effective medium (Tandon and Weng, 1984) and solved the Christoffel equation to determine quasi-SV and SH wave speeds (Walker and Wookey, 2012), from which we calculate ξ. We also tested other effective medium theories (e.g., Hudson, 1981), and found they give similar results.

For incoming S-waves with an incident angle of $20°$, we modeled the variation of ξ as a function of four factors: the aspect ratio (minor axis over major axis) of the intrusion, the velocity contrast between the intrusion and the background matrix, the volume fraction of the intrusions, and the relationship between the orientation of the intrusions and the propagation azimuth of the incoming S-wave. Three example models are shown in Fig. 7c, representing dry gas-filled ($V_P = 0.24$ km/s, $V_S = 0$ km/s, i.e., carbon dioxide) or water-filled ($V_P = 1.5$ km/s, $V_S = 0$ km/s) cracks/fractures (i.e., intrusions with a significantly reduced seismic velocity), and intrusions with a faster seismic velocity ($V_P = 6.3$ km/s, $V_S = 3.4$ km/s, e.g., frozen igneous dikes with a larger wave speed than the porous rocks). All of these reproduce ξ values compatible with our observation, however, there are significant trade-offs between the input parameters. For example, Fig. 7d shows the range of aspect ratios and volume fractions associated with low- and high-velocity intrusions that can reproduce the observation: larger aspect ratio intrusions require significantly higher volume fractions to exhibit sufficient anisotropy. Furthermore, models incorporating seismically fast intrusions need considerably higher volume fractions to reproduce the data. For example, to exhibit similar anisotropy (in Fig. 7c), the volume fraction is required to be 0.5% and 10% for low- and high-velocity intrusions, respectively.

A common feature of all the anisotropy models tested is that there is a strong dependence on the propagation azimuth of the incoming S-wave. For azimuths close to the strike direction of the intrusions, all the models show $\xi < 1$, whereas for azimuths closer to perpendicular this switches to $\xi > 1$. In reality, for intermediate angles (at non-horizontal incidence) the two shear-waves are not strictly horizontally or vertically polarized and would more likely appear isotropic than the strongly discontinuous variation suggested by the curve. In other words, anisotropy of the kind

(a)

(b)

(c)

(d)
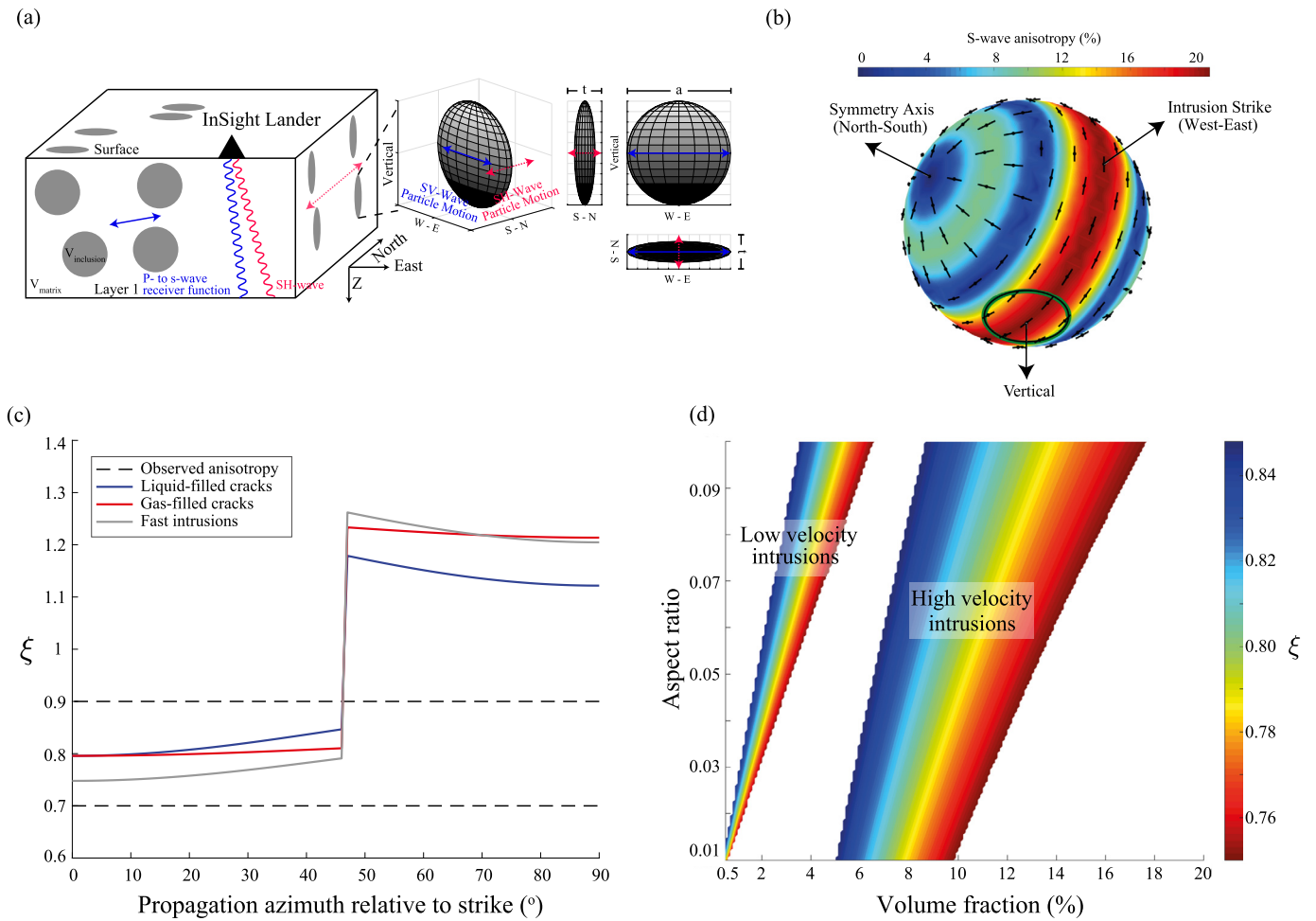
Fig. 7. Proposed mechanism for the measured anisotropy in Layer 1 at the InSight lander site. (a) The left panel shows an isotropic background matrix including isotropic disk-like inclusions (in grey). The black triangle represents the InSight lander, and the blue and red lines mark the incoming ray paths for the P- to s-wave receiver function and SH-wave reflection, respectively. The blue and red arrows denote their polarization directions (SV-wave in the Z-E plane, and SH-wave along the N-S direction). The composite is transversely anisotropic with a symmetry axis along the N-S direction. The right panels present details on the ellipsoidal inclusion, where t and a are the minor and major axes. (b) S-wave anisotropy and orientation of fast shear-wave for an example model of low-velocity (liquid) inclusions following theory of Tandon and Weng (1984). The green circle denotes the range of wave propagation azimuths modeled, with an incident angle of 20°. Color scale indicates difference between fast and slow shear-wave velocities. (c) Radial anisotropy coefficient, $\xi = (V_{SH}/V_{SV})^2$, for three example models representing fractures (liquid- or gas-filled, blue and red curves, respectively), and high velocity (e.g., igneous) intrusions (grey curve) with constraints from observation (grey dashed lines). All models have aspect ratios of 0.01, and volume fractions of 0.5% (low velocity intrusions) and 10% (high velocity). (d) Trade-off between parameters adopted in models. The color scale shows the modeled ξ as a function of the inclusion aspect ratio and volume fraction.

modeled would not be readily apparent in the data at these azimuths. This is a limitation of the measurement approach rather than the modeling itself. Thus, it is clear that to reproduce the observed signal, the intrusions should be oriented approximately East-West, close to the sagittal plane of the marsquakes interpreted as originating from the East.

There are several plausible explanations for these models. Regional compressive stress in the crust is expected to preferentially close fractures quasi-normal to the direction of maximum compression (e.g., Kaneshima, 1990; Boness and Zoback, 2006). The region of western Elysium Planitia around the InSight location (Fig. 1a and 1b) shows evidence of approximately North-South trending 'wrinkle ridges' (Golombek et al., 2018, 2020). Wrinkle ridges result from the thrust faulting and folding of sub-regolith lava flows resulting from compressive stress, (e.g., Mueller and Golombek, 2004; Golombek and Phillips, 2010). This suggests an approximately East-West compression direction, which would preferentially close North-South trending fractures leaving East-West fractures open. Dry- or liquid-filled fractures representing a sufficient volume fraction could produce the observed anisotropy. The potential sources of regional stresses in the crust include lithospheric loading from the Elysium and Tharsis volcanic provinces (Banerdt et al., 1982; Hall et al., 1986) that might be modulated by global compression (e.g., Mangold et al., 2000; Golombek and Phillips, 2010; Ruj and Kawai, 2021).

A second possible mechanism to reproduce the observed anisotropy is allowed by the potential for high-velocity intrusions in the crust. One explanation for such a model might be the presence of dike structures in the crust, from melting or volcanic events. Dike structures have been invoked as a mechanism for seismic anisotropy on Earth (e.g., Snyder and Bruneton, 2007; Lee et al., 2021). Dike structures are associated with a range of geologic events including impact cratering: radial and concentric diking are observed around known impact craters on Earth (e.g., Lambert, 1981; Head and Mustard, 2006) formed by impact melting. The InSight lander is on the western edge of a large (~175 km diameter, see Fig. 1b) quasi-circular depression, interpreted as a degraded, buried impact crater of approximately Noachian age (Golombek et al., 2018). Radial dikes associated with this crater would have an approximately East-West orientation beneath InSight, providing a second possible contributing mechanism to the observed anisotropy. Such a mechanism also provides an additional

explanation for extensive faulting and fracturing in the crust below InSight.

A joint inversion with the constraints from density studies (e.g., Baratoux et al., 2014; Knapmeyer-Endrun et al., 2021) could help better determine the aspect ratio, wave speed, and volume fraction of the intrusions in the future, potentially enabling us to distinguish between these mechanisms.

5. Conclusions

We have made the first detection of SH-wave reflections on the tangential component for broadband and low-frequency marsquakes (quality-A) with epicentral distances smaller than 60 degrees, which helps us constrain the crust at the lander site. Specifically, we found coherent signals from five events that appear to be independent of the focal depth and are consistent with SH-wave reflections off the first crustal interface (Layer 1). This phase confirms the existence of the ~8 km interface in the crust and the large wave speed (or impedance) contrast across it.

The range of acceptable parameters determined from the analysis of SH-waves does not intersect with the majority of the models from a previous RF study, which constrains the speed of SV waves (Knapmeyer-Endrun et al., 2021). We propose that this inconsistency results from the presence of seismic anisotropy within the top crustal layer at the lander site. Modeling results show that dry or liquid-filled cracks/fractures, and igneous intrusions can reproduce the observed radial anisotropy ($V_{SH} < V_{SV}$). A joint inversion with the constraints from density studies could help better determine the aspect ratio, wave speed, and volume fraction of the intrusions in the future, potentially enabling us to distinguish between these mechanisms. More high-quality marsquakes with a larger range of back-azimuth variation would help further study the azimuthal anisotropy and better contain the elastic properties of the Martian crust.

CRediT authorship contribution statement

Jiaqi Li: Conceptualization, Data curation, Formal analysis, Investigation, Methodology, Software, Validation, Visualization, Writing – original draft, Writing – review & editing. **Caroline Beghein:** Conceptualization, Formal analysis, Funding acquisition, Investigation, Methodology, Project administration, Supervision, Writing – original draft, Writing – review & editing. **James Wookey:** Methodology, Software, Validation, Visualization, Writing – review & editing. **Paul Davis:** Data curation, Formal analysis, Methodology, Resources, Software, Validation, Visualization, Writing – review & editing. **Philippe Lognonné:** Data curation, Resources, Writing – review & editing. **Martin Schimmel:** Formal analysis, Validation, Writing – review & editing. **Eleonore Stutzmann:** Formal analysis, Validation, Writing – review & editing. **Matthew Golombek:** Validation, Writing – review & editing. **Jean-Paul Montagner:** Validation, Writing – review & editing. **William Bruce Banerdt:** Writing – review & editing.

Declaration of competing interest

The authors declare that they have no known competing financial interests or personal relationships that could have appeared to influence the work reported in this paper.

Acknowledgements

Appendix A. Supplementary material

Supplementary material related to this article can be found online at https://doi.org/10.1016/j.epsl.2022.117654.

References

Acevedo, J., Fernández-Viejo, G., Llana-Fúnez, S., López-Fernández, C., Olona, J., Pérez-Millán, D., 2022. Radial anisotropy and S-wave velocity depict the internal to external zone transition within the Variscan orogen (NW Iberia). Solid Earth 13 (3), 659–679.

Banerdt, W., Phillips, R., Sleep, N., Saunders, R., 1982. Thick shell tectonics on one-plate planets: applications to Mars. J. Geophys. Res., Solid Earth 87 (B12), 9723–9733.

Banerdt, W.B., Smrekar, S.E., Banfield, D., Giardini, D., Golombek, M., Johnson, C.L., Lognonné, P., Spiga, A., Spohn, T., Perrin, C., Stähler, S.C., 2020. Initial results from the InSight mission on Mars. Nat. Geosci. 13 (3), 183–189.

Baratoux, D., Samuel, H., Michaut, C., Toplis, M.J., Monnereau, M., Wieczorek, M., Garcia, R., Kurita, K., 2014. Petrological constraints on the density of the martian crust. J. Geophys. Res., Planets 119 (7), 1707–1727.

Bastow, I., Pilidou, S., Kendall, J.-M., Stuart, G., 2010. Melt-induced seismic anisotropy and magma assisted rifting in Ethiopia: evidence from surface waves. Geochem. Geophys. Geosyst. 11 (6).

Beyreuther, M., Barsch, R., Krischer, L., Megies, T., Behr, Y., Wassermann, J., 2010. ObsPy: a Python toolbox for seismology. Seismol. Res. Lett. 81 (3), 530–533.

Boness, N.L., Zoback, M.D., 2006. Mapping stress and structurally controlled crustal shear velocity anisotropy in California. Geology 34 (10), 825–828.

Brinkman, N., Stähler, S.C., Giardini, D., Schmelzbach, C., Khan, A., Jacob, A., Fuji, N., Perrin, C., Lognonné, P., Beucler, E., et al., 2021. First focal mechanisms of marsquakes. J. Geophys. Res., Planets 126 (4), e2020JE006546.

Ceylan, S., Clinton, J., Giardini, D., Boese, M., Charalambous, C., van Driel, M., Horleston, A., Kawamura, T., Khan, A., Orhand-Mainsant, G., Scholz, J.R., 2021. Companion guide to the marsquake catalog from InSight, Sols 0–478: data content and non-seismic events. Phys. Earth Planet. Inter. 310, 106597.

Clifford, S.M., Lasue, J., Heggy, E., Boisson, J., McGovern, P., Max, M.D., 2010. Depth of the Martian cryosphere: revised estimates and implications for the existence and detection of subpermafrost groundwater. J. Geophys. Res., Planets 115 (E7).

Clinton, J.F., Ceylan, S., van Driel, M., Giardini, D., Stähler, S.C., Böse, M., Charalambous, C., Dahmen, N.L., Horleston, A., Kawamura, T., et al., 2021. The marsquake catalogue from InSight, sols 0–478. Phys. Earth Planet. Inter. 310, 106595.

Compaire, N., Margerin, L., Garcia, R.F., Pinot, B., Calvet, M., Orhand-Mainsant, G., Kim, D., Lekic, V., Tauzin, B., Schimmel, M., et al., 2021. Autocorrelation of the ground vibrations recorded by the seis-insight seismometer on Mars. J. Geophys. Res., Planets 126 (4), e2020JE006498.

Dreiling, J., Tilmann, F., Yuan, X., Giese, J., Rindraharisaona, E.J., Rümpker, G., Wysession, M.E., 2018. Crustal radial anisotropy and linkage to geodynamic processes: a study based on seismic ambient noise in southern Madagascar. J. Geophys. Res., Solid Earth 123 (6), 5130–5146.

Edwards, C.S., Nowicki, K.J., Christensen, P.R., Hill, J., Gorelick, N., Murray, K., 2011. Mosaicking of global planetary image datasets: 1. Techniques and data processing for Thermal Emission Imaging System (THEMIS) multi-spectral data. J. Geophys. Res., Planets 116 (E10).

Giardini, D., Lognonné, P., Banerdt, W.B., Pike, W.T., Christensen, U., Ceylan, S., Clinton, J.F., van Driel, M., Stähler, S.C., Böse, M., et al., 2020. The seismicity of Mars. Nat. Geosci. 13 (3), 205–212.

Golombek, M., Grott, M., Kargl, G., Andrade, J., Marshall, J., Warner, N., Teanby, N.A., Ansan, V., Hauber, E., Voigt, J., et al., 2018. Geology and physical properties investigations by the InSight lander. Space Sci. Rev. 214 (5), 1–52.

Golombek, M., Warner, N., Grant, J., Hauber, E., Ansan, V., Weitz, C., Williams, N., Charalambous, C., Wilson, S., DeMott, A., et al., 2020. Geology of the insight landing site on Mars. Nat. Commun. 11 (1), 1–11.

Golombek, M.P., Phillips, R.J., 2010. Mars tectonics. In: Watters, T.R., Schultz, R.A. (Eds.), Planetary Tectonics. Cambridge University Press, Cambridge, pp. 183–232 (Chap. 5).

Goossens, S., Sabaka, T.J., Genova, A., Mazarico, E., Nicholas, J.B., Neumann, G.A., 2017. Evidence for a low bulk crustal density for Mars from gravity and topography. Geophys. Res. Lett. 44 (15), 7686–7694.

Hall, J.L., Solomon, S.C., Head, J.W., 1986. Elysium region, Mars: tests of lithospheric loading models for the formation of tectonic features. J. Geophys. Res., Solid Earth 91 (B11), 11377–11392.

Hauck, S.A., Phillips, R.J., 2002. Thermal and crustal evolution of Mars. J. Geophys. Res., Planets 107 (E7), 6-1–6-19.

Head, J.W., Mustard, J.F., 2006. Breccia dikes and crater-related faults in impact craters on Mars: erosion and exposure on the floor of a crater 75 km in diameter at the dichotomy boundary. Meteorit. Planet. Sci. 41 (10), 1675–1690.

Hudson, J.A., 1981. Wave speeds and attenuation of elastic waves in material containing cracks. Geophys. J. Int. 64 (1), 133–150.

InSight Marsquake Service, 2020. Mars Seismic Catalogue, InSight Mission; V1.

InSight Marsquake Service, 2021a. Mars Seismic Catalogue, InSight Mission; V7.

InSight Marsquake Service, 2021b. Mars Seismic Catalogue, InSight Mission; V8.

InSight Marsquake Service, 2022a. Mars Seismic Catalogue, InSight Mission; V9.

InSight Marsquake Service, 2022b. Mars Seismic Catalogue, InSight Mission; V10.

InSight Mars SEIS Data Service, 2019. SEIS Raw Data, Insight Mission. IPGP, JPL, CNES, ETHZ, ICL, MPS, ISAE-Supaero, LPG, MFSC.

InSight SEIS Data Bundle, 2021. PDS Geosciences (GEO) Node.

Johnson, B.C., Milliken, R.E., Lewis, K.W., Collins, G.S., 2021. Impact generated porosity in Gale crater and implications for the density of sedimentary rocks in lower Aeolis Mons. Icarus 366, 114539.

Kaneshima, S., 1990. Origin of crustal anisotropy: shear wave splitting studies in Japan. J. Geophys. Res., Solid Earth 95 (B7), 11121–11133.

Kennett, B.L.N., 2009. Seismic Wave Propagation in Stratified Media. ANU Press.

Knapmeyer-Endrun, B., Panning, M.P., Bissig, F., Joshi, R., Khan, A., Kim, D., Lekic, V., Tauzin, B., Tharimena, S., Plasman, M., et al., 2021. Thickness and structure of the martian crust from InSight seismic data. Science 373 (6553), 438–443.

Lambert, P., 1981. Breccia dikes—geological constraints on the formation of complex craters. In: Multi-Ring Basins: Formation and Evolution. Pergamon Press, New York, pp. 59–78.

Langston, C.A., 1979. Structure under Mount Rainier, Washington, inferred from teleseismic body waves. J. Geophys. Res., Solid Earth 84 (B9), 4749–4762.

Lee, S.-J., Kim, S., Rhie, J., Kang, T.-S., Kim, Y., 2021. Upper crustal shear wave velocity and radial anisotropy beneath Jeju Island volcanoes from ambient noise tomography. Geophys. J. Int. 225 (2), 1332–1348.

Liu, M., Ritsema, J., Chaves, C., in preparation. Influence of shear-wave velocity heterogeneity on SH wave reverberation imaging of the mantle transition zone. Geophys. J. Int.

Liu, T., Shearer, P.M., 2021. Complicated lithospheric structure beneath the contiguous US revealed by teleseismic reflections. J. Geophys. Res., Solid Earth 126 (5), e2020JB021624.

Lognonné, P., Banerdt, W.B., Giardini, D., Pike, W.T., Christensen, U., Laudet, P., De Raucourt, S., Zweifel, P., Calcutt, S., Bierwirth, M., Hurst, K.J., 2019. SEIS: insight's seismic experiment for internal structure of Mars. Space Sci. Rev. 215 (1).

Lognonné, P., Banerdt, W., Pike, W., Giardini, D., Christensen, U., Garcia, R.F., Kawamura, T., Kedar, S., Knapmeyer-Endrun, B., Margerin, L., et al., 2020. Constraints on the shallow elastic and anelastic structure of Mars from InSight seismic data. Nat. Geosci. 13 (3), 213–220.

Manga, M., Wright, V., 2021. No cryosphere-confined aquifer below InSight on Mars. Geophys. Res. Lett. 48 (8), e2021GL093127.

Mangold, N., Allemand, P., Thomas, P., Vidal, G., 2000. Chronology of compressional deformation on Mars: evidence for a single and global origin. Planet. Space Sci. 48 (12–14), 1201–1211.

Mueller, K., Golombek, M., 2004. Compressional structures on Mars. Annu. Rev. Earth Planet. Sci. 32, 435–464.

Pan, L., et al., 2020. Crust stratigraphy and heterogeneities of the first kilometers at the dichotomy boundary in western Elysium Planitia and implications for InSight lander. Icarus 338, 113511.

Plesa, A.-C., Padovan, S., Tosi, N., Breuer, D., Grott, M., Wieczorek, M., Spohn, T., Smrekar, S., Banerdt, W., 2018. The thermal state and interior structure of Mars. Geophys. Res. Lett. 45 (22), 12–198.

Ruj, T., Kawai, K., 2021. A global investigation of wrinkle ridge formation events; implications towards the thermal evolution of Mars. Icarus 369, 114625.

Savage, M.K., 1999. Seismic anisotropy and mantle deformation: what have we learned from shear wave splitting? Rev. Geophys. 37 (1), 65–106.

Schimmel, M., Stutzmann, E., Lognonné, P., Compaire, N., Davis, P., Drilleau, M., Garcia, R., Kim, D., Knapmeyer-Endrun, B., Lekic, V., et al., 2021. Seismic noise autocorrelations on Mars. Earth Space Sci., e2021EA001755.

Scholz, J.-R., Widmer-Schnidrig, R., Davis, P., Lognonné, P., Pinot, B., Garcia, R.F., Hurst, K., Pou, L., Nimmo, F., Barkaoui, S., et al., 2020. Detection, analysis, and removal of glitches from InSight's seismic data from Mars. Earth Space Sci. 7 (11), e2020EA001317.

Shearer, P.M., 2019. Introduction to Seismology. Cambridge University Press.

Shearer, P.M., Buehler, J., 2019. Imaging upper-mantle structure under USarray using long-period reflection seismology. J. Geophys. Res., Solid Earth 124 (9), 9638–9652.

Silver, P.G., Chan, W.W., 1988. Implications for continental structure and evolution from seismic anisotropy. Nature 335 (6185), 34–39.

Smith, D.E., Zuber, M.T., Frey, H.V., Garvin, J.B., Head, J.W., Muhleman, D.O., Pettengill, G.H., Phillips, R.J., Solomon, S.C., Zwally, H.J., Banerdt, W.B., 2001. Mars Orbiter Laser Altimeter: experiment summary after the first year of global mapping of Mars. J. Geophys. Res., Planets 106 (E10), 23689–23722.

Snyder, D., Bruneton, M., 2007. Seismic anisotropy of the slave craton, NW Canada, from joint interpretation of SKS and Rayleigh waves. Geophys. J. Int. 169 (1), 170–188.

Stähler, S.C., Khan, A., Banerdt, W.B., Lognonné, P., Giardini, D., Ceylan, S., Drilleau, M., Duran, A.C., Garcia, R.F., Huang, Q., et al., 2021. Seismic detection of the martian core. Science 373 (6553), 443–448.

Tandon, G.P., Weng, G.J., 1984. The effect of aspect ratio of intrusions on the elastic properties of unidirectionally aligned composites. Polym. Compos. 5 (4), 327–333.

Volk, O., White, R.S., Pilia, S., Green, R.G., Maclennan, J., Rawlinson, N., 2021. Oceanic crustal flow in Iceland observed using seismic anisotropy. Nat. Geosci. 14 (3), 168–173.

Walker, A.M., Wookey, J., 2012. MSAT—a new toolkit for the analysis of elastic and seismic anisotropy. Comput. Geosci. 49, 81–90.

Wang, R., 1999. A simple orthonormalization method for stable and efficient computation of Green's functions. Bull. Seismol. Soc. Am. 89 (3), 733–741.